ACS APPLIED MATERIALS & INTERFACES

Research Article

www.acsami.org

Controlled Growth and Atomic-Scale Mapping of Charged Heterointerfaces in $PbTiO_3/BiFeO_3$ Bilayers

Ying Liu,[†,‡] Yin-Lian Zhu,*[,†] Yun-Long Tang,[†] Yu-Jia Wang,[†] Shuang Li,[†,‡] Si-Rui Zhang,[†,‡] Meng-Jiao Han,[†,‡] Jin-Yuan Ma,[†,§] Jagadeesh Suriyaprakash,[†,‡] and Xiu-Liang Ma[†,§]

[†]Shenyang National Laboratory for Materials Science, Institute of Metal Research, Chinese Academy of Sciences, Wenhua Road 72, 110016 Shenyang, China

[‡]University of Chinese Academy of Sciences, Yuquan Road 19, 100049 Beijing, China

[§]School of Materials Science and Engineering, Lanzhou University of Technology, Langongping Road 287, 730050 Lanzhou, China

ABSTRACT: Functional oxide interfaces have received a great deal of attention owing to their intriguing physical properties induced by the interplay of lattice, orbital, charge, and spin degrees of freedom. Atomic-scale precision growth of the oxide interface opens new corridors to manipulate the correlated features in nanoelectronics devices. Here, we demonstrate that both head-to-head positively charged and tail-to-tail negatively charged $BiFeO_3/PbTiO_3$ (BFO/PTO) heterointerfaces were successfully fabricated by designing the BFO/PTO film system deliberately. Aberration-corrected scanning transmission electron microscopic mapping reveals a head-to-head polarization configuration present at the BFO/PTO interface, when the film was deposited directly on a $SrTiO_3$ (001) substrate. The interfacial atomic structure is reconstructed, and the interfacial width is determined to be 5−6 unit cells. The polarization on both sides of the interface is remarkably enhanced. Atomic-scale structural and chemical element analyses exhibit that the reconstructed interface is rich in oxygen, which effectively compensates for the positive bound charges at the head-to-head polarized BFO/PTO interface. In contrast to the head-to-head polarization configuration, the tail-to-tail BFO/PTO interface exhibits a perfect coherency, when $SrRuO_3$ was introduced as a buffer layer on the substrates prior to the film growth. The width of this tail-to-tail interface is estimated to be 3−4 unit cells, and oxygen vacancies are supposed to screen the negative polarization bound charge. The formation mechanism of these distinct interfaces was discussed from the perspective of charge redistribution.

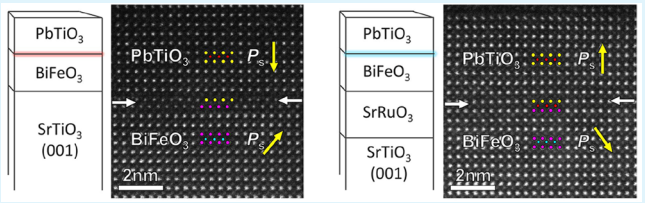

KEYWORDS: *charged interface, perovskite, ferroelectric, controlled growth, STEM*

1. INTRODUCTION

Correlated oxide interfaces are an arena of both great interest and challenge. The coupling of lattice, orbital, charge, and spin degrees of freedom at oxide interfaces gives rise to multiple functionalities, such as two-dimensional (2D) electron gas,[1] superconductivity,[2] magnetoelectric coupling,[3−5] and so forth. Ferroelectrics, which feature a spontaneous electric polarization, can modulate the interfacial electric and magnetic behaviors appropriately by monitoring their polarization directions, when they form functional interfaces with other components such as ferromagnetics and metals.[6,7] Particularly, ferroelectric spontaneous polarization directions can modify the electron transport behavior and yield distinct conductance states of a ferroelectric tunneling junction, suggesting potential applications in high-density data storage.[7,8] Furthermore, spin polarization can be engineered by ferroelectric polarization directions via a magnetoelectric coupling effect at the ferroelectric/ferromagnet interface, which is widely identified in ferroelectric tunnel junctions with ferromagnetic electrodes.[4,9]

Ferroelectric domain walls, separating different orientations of electric polarizations, are homogeneous interfaces with unique physical behaviors such as conduction, magnetotransport, photovoltaic effect, and so forth.[10−17] These interfaces exhibit head-to-tail, head-to-head, and tail-to-tail polarization configurations, which will introduce zero, net positive, and net negative bound charges, respectively. In particular, charged domain walls may facilitate the accumulation of free charge carriers and lead to a metallic conduction with respect to the common uncharged ones;[18] such a conduction has been observed experimentally in $Pb(Zr_{0.2}Ti_{0.8})O_3$, $ErMnO_3$, $LiNbO_3$, and $BaTiO_3$.[13,14,19,20] Moreover, an improved electromechanical response was reported at charged domain walls in $BaTiO_3$, believed to be driven by incomplete screening of bound charge at the domain walls, which creates a stable depolarizing field across each domain.[21] These interfaces, as various functional entities, show tremendous potential applications especially if they can be fabricated precisely at the atomic scale. In recent years, the atomic details of these domain walls have been explored profoundly using aberration-corrected transmission

Received: April 2, 2017
Accepted: July 5, 2017
Published: July 5, 2017

DOI: 10.1021/acsami.7b04681
ACS Appl. Mater. Interfaces 2017, 9, 25578−25586

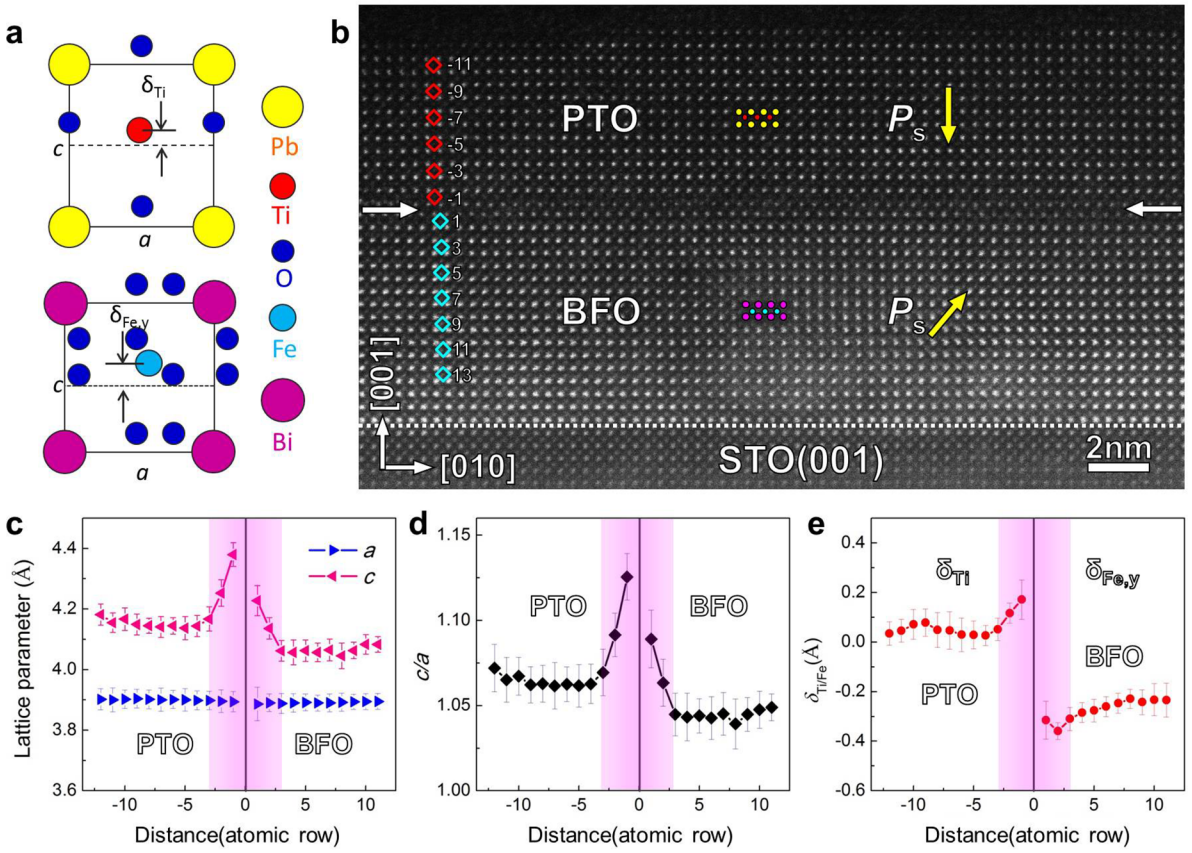

Figure 1. Configuration of a head-to-head polarized $BiFeO_3/PbTiO_3$ (BFO/PTO) heterointerface. (a) Projected schematics of PTO and BFO crystals along the [100] direction. (b) A HAADF-STEM image of a BFO/PTO film grown on a STO (001) substrate. PTO and BFO crystal structures are superimposed on the HAADF-STEM image. (Yellow circles, Pb; red, Ti; pink, Bi; blue, Fe.) Yellow arrows in the BFO and PTO layers denote P_s directions. White arrows and white dotted lines indicate the BFO/PTO and BFO/STO interface, respectively. (c) In-plane (a) and out-of-plane (c) lattice parameter curves extracted from the corresponding atomic rows (labeled as numbers and hollow diamonds) in the image (b). (d), (e) Tetragonality (c/a) and Ti/Fe ion displacement ($\delta_{Ti/Fe}$) curves of the BFO/PTO film. Black long strings located at zero in images (b–d) indicate the BFO/PTO interface, while the pink semitransparent area manifests the width of the head-to-head BFO/PTO interface.

electron microscopy, and their structural (lattice parameters, tetragonality, etc.) and electric (ferroelectric ions displacement, spontaneous polarization) parameters show significant differences, which provide insights into the various enticing phenomena found at the domain walls from the structural perspective.[22−25]

Interfaces between two ferroelectrics, separating not only domains with different polarization directions (or polarization magnitude) but also materials with different element constituents, exhibit a combined characteristic of both ferroelectric domain walls and heterointerfaces. These interfaces could largely modify the properties of the film system.[26,27] Particularly, strong magnetoelectric coupling was revealed at $BaTiO_3/BiFeO_3$ interfaces, which is useful for novel spintronic and magnetoelectric device applications.[28−31] Furthermore, giant piezoelectric performances were demonstrated in $CaTiO_3/PbTiO_3$ and $BaTiO_3/PbTiO_3$ superlattices by engineering ferroelectric polarization rotations through heterointerfaces.[32,33] Nevertheless, though these kinds of unique properties have been observed and studied in these ferroelectric/ferroelectric systems, the atomic details and interfacial charge behavior (which play significant roles in determining their physical properties) have not yet been studied clearly. To shed more light on this issue and to provide knowledge about the heterointerface system at the atomic level, here we design a multiferroic/ferroelectric $BiFeO_3/PbTiO_3$ (BFO/PTO) film system with both having a large spontaneous polarization (P_s). This film system exhibits discontinuities not only in ferroelectric polarization but also in chemical valence ($(PbO)^0$, $(TiO_2)^0$, $(BiO)^+$, $(FeO_2)^-$). Because of this unique charge state, a giant enhancement of ferroelectric polarization has been identified near head-to-tail polarized interfaces with terminated FeO_2/PbO planes in our previous study.[34] In this work, head-to-head positively charged and tail-to-tail negatively charged BFO/PTO interfaces were successfully fabricated using the pulsed laser deposition (PLD) technique by designing the film system properly. Using aberration-corrected scanning transmission electron microscopy (STEM), which is powerful in investigating the heterointerfaces[35,36] and novel topological domain configurations[37,38] of complex oxides, the differences in both the structural and electrical parameters of these two heterointerfaces have been investigated at the atomic scale, suggesting the potential possibilities of distinct properties.

2. EXPERIMENTAL SECTION

2.1. Materials. Two kinds of BFO/PTO thin films were grown on a $SrTiO_3$ (STO) substrate by the PLD technique without and with a predeposition of $SrRuO_3$ (SRO) buffer layer, using a Coherent ComPexPRO 201FKrF (λ = 248 nm) excimer laser. During the growth of SRO, the stoichiometric target was used; while the 3 mol % Pb-rich and Bi-rich ceramic targets were used to grow PTO and BFO thin films. While growing SRO at the laser energy of 280 mJ, the

DOI: 10.1021/acsami.7b04681
ACS Appl. Mater. Interfaces 2017, 9, 25578−25586

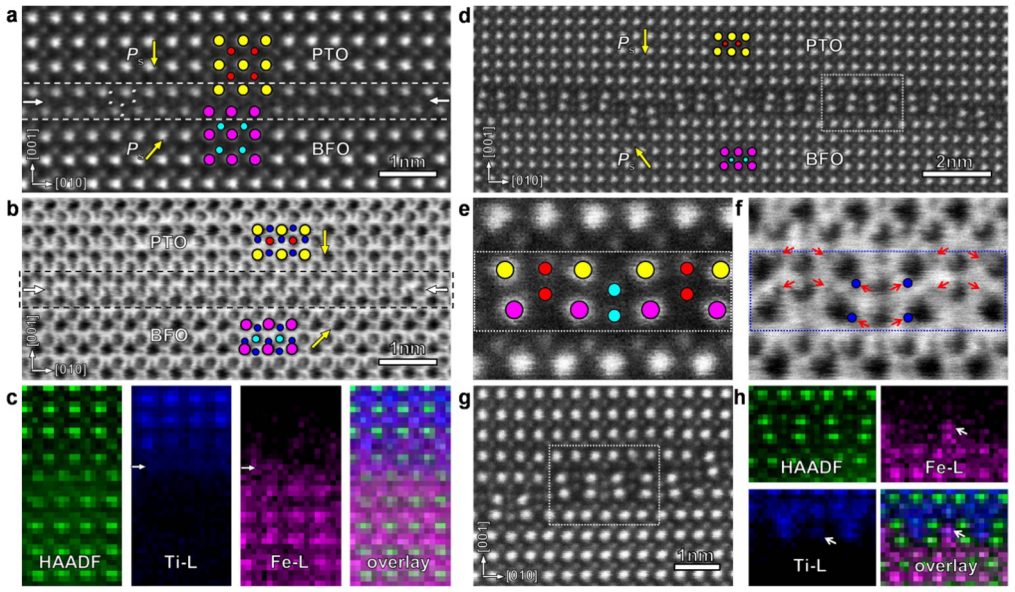

Figure 2. Investigation of the BFO/PTO interface structure corresponds to that in Figure 1. (a, b) Enlarged HAADF- and BF-STEM images of Figure 1a. (c) EELS elemental maps. HAADF, Ti, and Fe signals are shown in green, navy blue, and pink, respectively. The one labeled as overlay is a color mixture of HAADF, Ti-L, and Fe-L signals. (d) A HAADF-STEM image of the BFO/PTO interface that shows another interfacial atomic configuration. (e, f) Further enlarged HAADF- and BF-STEM images of the interface structure of the rectangular area in the image (d). In the HAADF image (image (e)), the brightest spots are Pb/Bi columns, while those with weak contrast correspond to Ti/Fe columns. In the BF-STEM image (image (f)), the extra spots (compare with HAADF image) are determined to be oxygen columns, which are indicated by red arrows. (g) An enlarged HAADF-STEM image. (h) EELS elemental maps correspond to the rectangular area in (e).

background oxygen pressure was maintained at 50 mTorr. The substrate temperature and a laser repetition rate were fixed as 700 °C and 4 Hz, respectively. For the deposition of BFO, an oxygen pressure of 90 mTorr, a substrate temperature of 800 °C, a laser repetition of 6 Hz, and a laser energy of 350 mJ were employed; for PTO, the parameters were adjusted to 90 mTorr, 700 °C, 4 Hz, and 310 mJ. After growth, the film was annealed at 700 °C in an oxygen pressure of 0.5 atm for 10 min and then cooled to room temperature slowly at a rate of 5 °C/min.

2.2. TEM Sample Preparation, High Angle Annular Dark Field/Bright Field (HAADF/BF) STEM and Electron Energy Loss Spectroscopy (EELS) Elemental Map. Cross-sectional samples oriented along STO [100] direction for STEM observation were prepared by conventional slicing, gluing, grinding, polishing, and finally ion milling. All STEM and EELS results were acquired by employing an aberration-corrected scanning transmission electron microscope (Titan Cubed 60−300 kV microscope (FEI) equipped with an image corrector and a probe corrector from CEOS, high-brightness field-emission gun (X-FEG), and a monochromator) operating at 300 kV. HAADF/BF-STEM images were recorded with a convergence semiangle of 21.4 mrad. EELS elemental map data across the BFO/PTO interface was acquired from 380 to 880 eV with a dispersion of 0.25 eV/ch and a collective angle of 85 mrad.

2.3. Determination of Ion Column Positions and $\delta_{Ti/Fe}$ Map. The atom column positions were determined by fitting them as 2D Gaussian peaks using the Matlab software.[23,24,39]

3. RESULTS AND DISCUSSION

PTO is a typical tetragonal ferroelectric with the lattice parameters of $a = b = 3.9$ Å and $c = 4.15$ Å. In a PTO unit cell, both Ti and O octahedrons displace from the center of the Pb lattice, giving rise to a spontaneous polarization along the c axis ([001] direction).[37,40] BFO is a multiferroic exhibiting both ferroelectric and antiferromagnetic orders, which has a distorted perovskite structure with the lattice parameters of $a_{pc} = b_{pc} = c_{pc} = 3.96$ Å ("pc" is an abbreviation for pseudocubic). In the BFO unit cell, Fe shifts slightly from the Bi lattice center along the pseudocubic [111] direction, and six oxygens form a distorted octahedron.[24,31,41,42] Projected crystal structures of PTO and BFO are schematically shown in Figure 1a, where yellow, red, pink, light blue, and navy blue circles denote Pb, Ti, Bi, Fe and O, respectively.

3.1. Head-to-Head Positively Charged BFO/PTO Heterointerface. Figure 1b is a HAADF-STEM image showing the BFO(~5 nm)/PTO(~5 nm) bilayered film with BFO grown directly on the STO (001) substrate, and then, PTO was grown on BFO. In this image, Pb/Bi show bright and Ti/Fe show weak contrast due to the large atomic number of Pb/Bi compared with Ti/Fe; the crystal structures of both PTO and BFO are superimposed on the HAADF image to show their structures clearly, where Pb, Bi, Fe, and Ti columns are in the corresponding colors as those in Figure 1a. It is noted that the interface is not perfectly coherent. A notable reconstructed BFO/PTO interface deviating from the typical perovskite structure is identified (indicated by two opposite white arrows), and a horizontal shift of half a perovskite unit cell is revealed across the interface. In both PTO and BFO layers, P_s directions (indicated by yellow arrows) are determined based on the opposite directions of Ti(Fe) ion displacements with respect to the mass center of its four nearest Pb(Bi), which has been widely used in previous reports.[23,25,41,43−47] Ti shifting upward corresponding to the Pb sublattice and Fe shifting downward with respect to its four nearest Bi (along out-of-plane direction) are clearly revealed; therefore, P_s directions in both BFO and PTO are determined to be pointed toward the BFO/PTO interface, forming a head-to-head charged interface. To further investigate the structural and electric characteristics of this reconstructed interface, in-plane (a, labeled as right triangle) and out-of-plane (c, labeled as left triangle) lattice parameters are extracted from the corresponding atomic rows of the HAADF image (labeled as hollow diamonds in Figure 1b) and shown in Figure 1c, where the vertical line at the zero position

DOI: 10.1021/acsami.7b04681
ACS Appl. Mater. Interfaces 2017, 9, 25578−25586

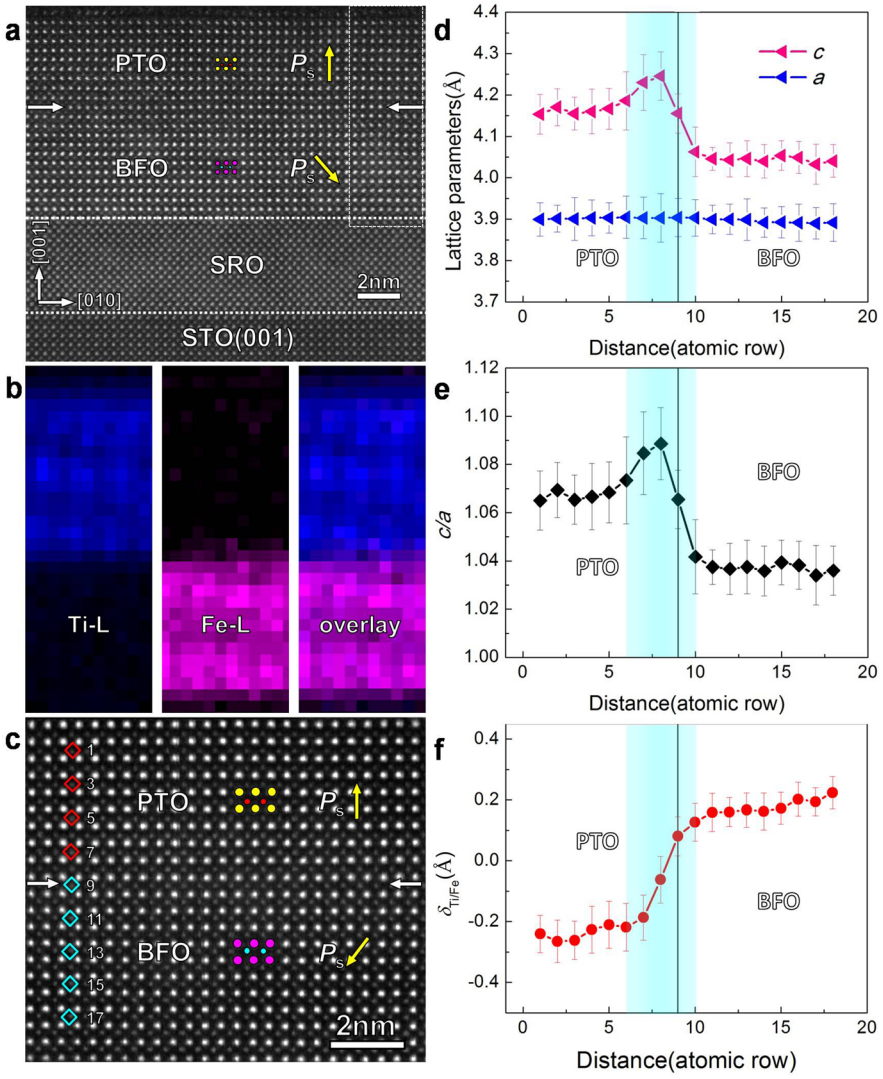

Figure 3. Configuration of the tail-to-tail polarized BFO/PTO interface. (a) A HAADF-STEM image of BFO/PTO film grown on the STO (001) substrate with a SRO buffer layer of ∼10 unit cell. White arrows indicate the BFO/PTO interface while yellow arrows indicate P_s directions. (b) EELS elemental map of the BFO/PTO film, where Ti is in navy blue and Fe is in pink. (c) Enlarged HAADF-STEM image of (a). (d) In-plane (a) and out-of-plane (c) lattice parameters profiles extracted from image (c). (e–f) Tetragonality (c/a) and Ti/Fe ion displacement ($\delta_{Ti/Fe}$) curves extracted from (c).

denotes the BFO/PTO interface. From this image, uniform in-plane lattice parameters are revealed in the whole film, whereas an obvious enlargement of out-of-plane lattice parameters is identified in the area near the BFO/PTO interfaces with the width of about 5–6 unit cells. At the position of the exact interface, c reaches a peak value as high as 4.4 Å. In parallel with the numbers in Figure 1b and the increase in out-of-plane lattice parameters, the corresponding tetragonality (c/a) is calculated and shown in Figure 1d, which further displays this enlargement tendency near the BFO/PTO interface. Meanwhile, the extracted data of both Ti displacement (δ_{Ti}, Ti displacement vector with respect to Pb) and Fe displacement ($\delta_{Fe,y}$, Fe displacement vector with respect to Bi along [001]) profiles are shown in Figure 1e, displaying an increasing trend of the δ_{Ti} and $\delta_{Fe,y}$ absolute values. The enlarged tetragonality associated with the increased δ_{Ti} displacements suggests an enhancement of polarization near the BFO/PTO interface. Considering the combination of structural and electric parameters shown in Figure 1b–d, the width of this reconstructed interface is estimated to be about 5–6 unit cells as indicated by the shadow areas. This width is of great difference from that of the head-to-head 180° domain wall reported previously in $PbZr_{0.2}Ti_{0.8}O_3$, which is estimated to be about 10 unit cells in thickness.[22] The reason for this difference will be discussed later.

To further analyze the atomic configuration of this reconstructed BFO/PTO interface, enlarged HAADF, BF-STEM imaging, and EELS elemental mapping were conducted, and the results are shown in Figure 2. From Figure 2a, Pb/Bi (bright contrast, yellow/pink circles) and Ti/Fe (weak contrast, red/light blue circles) columns can be determined in both the BFO and PTO layers. Nevertheless, at the exact interface (the area sandwiched by two horizontal dashed lines), only the brightest contrast can be clearly revealed to be Pb or Bi as denoted by yellow and pink circles (since it is difficult to distinguish between Pb and Bi using both the electron energy loss spectrum and energy dispersive X-ray spectroscopy, we suppose the brightest columns at the PTO side are Pb and those at the BFO side are Bi), while some other weak contrast (indicated by six small white arrows) may arise from Ti/Fe.

DOI: 10.1021/acsami.7b04681
ACS Appl. Mater. Interfaces 2017, 9, 25578–25586

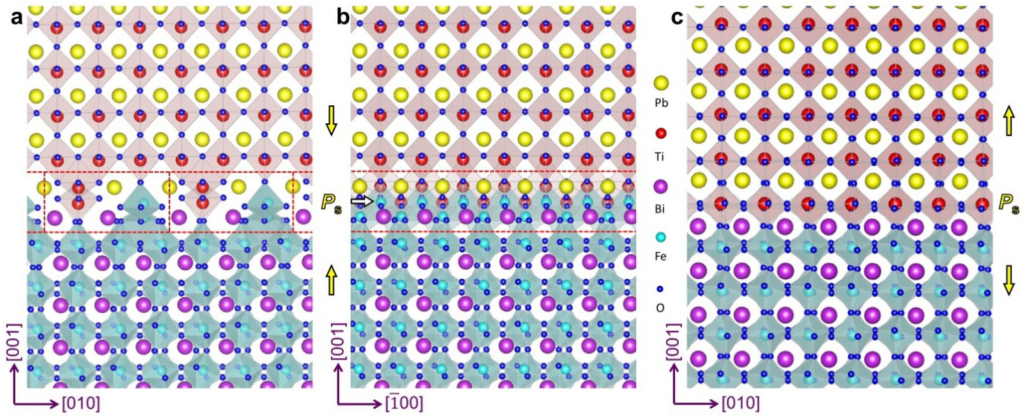

Figure 4. Atomic models of head-to-head (a, b) and tail-to-tail (c) polarized BFO/PTO interfaces, where yellow, red, purple, light blue, and navy blue circles indicate Pb, Ti, Bi, Fe, and O respectively; oxygen octahedrons in PTO and BFO are shown in pink and blue, respectively; yellow arrows indicate P_s directions; white arrow in (b) denote the BFO/PTO interface.

However, the remarkably weak intensity of Fe/Ti at the interface compared with those in the PTO or BFO layers suggests that the interface may contain lesser amounts of Ti or Fe. It is known that oxygen plays an important role in determining ferroelectric polarizations. To accurately quantify the structure-related parameters, BF-STEM observation was conducted to visualize oxygen atomic columns, and the results are shown in Figure 2b. In contrast with the HAADF image, atomic columns in the BF image show dark contrast upon a bright background. On the basis of a combination of HAADF and BF-STEM images, oxygen columns are determined to be the smallest dark image spots (navy blue circles) in Figure 2b. Through the positions of Pb/Bi, Ti/Fe, and O, P_s directions (yellow arrows) in both BFO and PTO can be further verified to point toward the BFO/PTO interface. However, the Ti/Fe columns are difficult to distinguish from O at the interface (between two black dashed lines), and they may be overlapped due to the chaos of atom redistribution at the interface. In addition to the atomic structure at the interface, chemical constituents were also investigated using EELS elemental mappings as shown in Figure 2c, which shows the HAADF image (green), Ti-L (navy blue), Fe-L (pink) signals, and an overlay of them. These elemental maps show a coexistence of Ti and Fe signals at the exact interface as indicated by white arrows. Furthermore, the nonuniform Fe-L signal is observed in the PTO layer, which may suggest some diffusion of Fe into the PTO layer.

In addition to the interfacial atomic configurations commonly observed in Figure 2a, we have also noticed another interface configuration featuring pairs of A-site ions (Pb or Bi) separated by pairs of B-site ions (Ti or Fe) as shown in Figure 2d. The vertical distance of the pair of A-site ions is estimated to be about 3 Å, which is about three-fourths of the perovskite unit cell. Similar atomic arrangements have previously been reported in $(Bi_{0.85}Nd_{0.15})(Ti_{0.1}Fe_{0.9})O_3$ solid solution by MacLaren et al., which appears at an antiphase boundary (APB) instead of a heterointerface.[48] To investigate the oxygen distribution at this interface, BF-STEM observation was conducted. Figure2e, f shows the enlarged HAADF and BF-STEM images of the same area, where A-site (bright spots in image (e)), B-site (weak spots in image (e)), and O (the small dark spots in image (f) indicated by red arrows) ion columns can be directly determined. Interfacial chemical information is also extracted by using the EELS technique. Figure2g is an enlarged HAADF-STEM image showing the details at the interface. Figure 2h is the elemental mappings of Fe-L signals, Ti-L signals, and the overlay corresponding to the rectangular area in image Figure2g. From the EELS maps, it is clear that the pairs of B-site ions, which are separated by pairs of A-site ions, are arranged with Fe and Ti ions stacking alternately. Some intermixing of Ti and Fe is also identified as indicated by white arrows.

3.2. Tail-to-Tail Negatively Charged BFO/PTO Heterointerface. Tail-to-tail polarized heterointerfaces were obtained in BFO(~5 nm)/PTO(~5 nm) bilayers grown on a STO (001) substrate with a predeposition of (~4 nm) SRO buffer layer. The introduction of the SRO buffer layer is to modify the P_s direction of BFO and make it point toward SRO (due to the work function difference between BFO and SRO).[49] A HAADF-STEM image of this film is shown in Figure 3a, where a uniform contrast along the whole PTO/BFO film is revealed. To accurately trace the position of the BFO/PTO interface, EELS element analysis was conducted, and the results are shown in Figure 3b, in which Ti-L maps, Fe-L maps, and their overlay (Ti and Fe) signal corresponding to the rectangular area in Figure 3a are shown. In this image, Ti and Fe are shown in navy blue and pink, respectively. A clear Fe signal at the downside layer and a Ti signal at the upside layer are identified, which verifies that the film on the SRO layer does contain both BFO and a PTO layers and the BFO/PTO interface showing a perfect coherency. To further analyze the interfacial structural and electric parameter information, an enlarged HAADF-STEM image is shown in Figure 3c, from which lattice parameters, tetragonality, and Ti/Fe ion displacement ($\delta_{Ti/Fe}$) are extracted (the corresponding atomic rows are labeled as hollow diamond and numbers in Figure 3c) and shown in Figure 3d–f. Lattice parameter profiles in Figure 3d display a uniform in-plane lattice parameter (a, about 3.9 Å) along the BFO/PTO film, while the out-of-plane lattice parameter is about 4.16 Å in PTO and 4.04 Å in BFO. Interestingly, the out-of-plane lattice parameters of PTO can reach 4.24 Å near the BFO/PTO interface, which suggests some unusual phenomena. The tetragonality profile shown in Figure 3e displays a similar tendency as that of the out-of-plane lattice parameter. The averaged tetragonality is estimated to be ~1.067 and ~1.036 in PTO and BFO, respectively, while that of PTO near the interface reaches 1.087. The Ti/Fe displacement curve is shown in Figure 3f, which shows a

DOI: 10.1021/acsami.7b04681
ACS Appl. Mater. Interfaces 2017, 9, 25578–25586

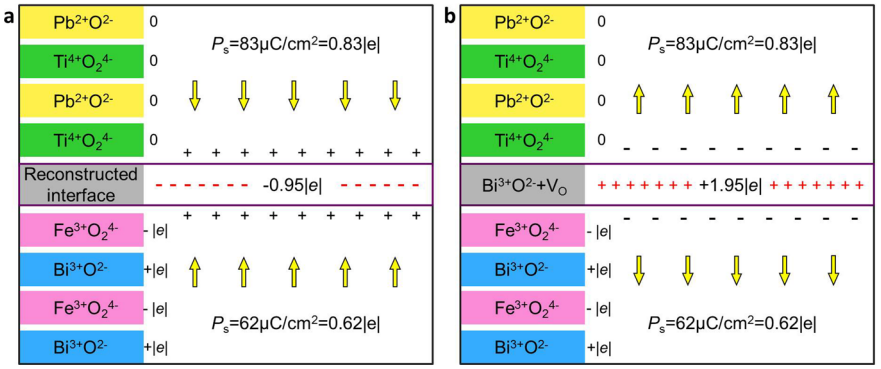

Figure 5. Schematics of charge configuration at head-to-head (a) and tail-to-tail (b) polarized BFO/PTO interfaces. "+" indicate positive charge while "−" indicate negative charge. Yellow arrows indicate P_s directions.

negative Ti displacement vector in PTO and a positive Fe displacement vector in the BFO layer, consistent with the tail-to-tail polarization configuration. These results shown above manifest a trend varying in the range of about 3−4 unit cells, which suggests a width of 3−4 unit cells for this tail-to-tail polarized interface.

3.3. Modeling and Charge Compensation Analysis of Head-to-Head and Tail-to-Tail BFO/PTO Interfaces. To understand the structure and the charge compensation phenomena at the head-to-head and tail-to-tail polarized BFO/PTO heterointerfaces, their structural models are built and shown in Figure4, where yellow, red, pink, light blue, and navy blue circles denote Pb, Ti, Bi, Fe, and O, respectively. The atomic models of the head-to-head polarized interface are shown in Figure 4a, b, which are both the reconstructed interface structure yet with orientations differing for 90°. This interfacial model is built based on the elemental analysis shown in Figure 2 and the structure reported by MacLaren et al.[48] in $(Bi_{0.85}Nd_{0.15})(Ti_{0.1}Fe_{0.9})O_3$. The atomic model in Figure 4a corresponds to the interfacial structure observed in Figure 2d−h, which manifests the atomic arrangement characteristic of the pairs of A-site ions separated by pairs of B-site ions. In this image, the area between two horizontal white dashed lines is defined as the exact interface, since a simple perovskite structure is adopted on both sides of this area (that is in BFO and PTO). The structural unit of the interface is labeled by the red dashed lines, which corresponds to three perovskite unit cells. The structural model shown in Figure 4b is constructed based on the results shown in Figure 2a−c. It can be revealed that atoms at the interface between two red lines arrange in a much complex manner, and the overlaying of O and Fe/Ti columns is clear. Moreover, both Fe and Ti coexist at the atom layer indicated by white arrows, agreeing well with the elemental analysis in Figure 2c. Figure 4c shows the structural model of the tail-to-tail interface corresponding to that in Figure 3. Since it is a coherence interface, its interfacial model is simple. In this model, we construct a $(BiO)^+/(TiO_2)^0$ interface. This interfacial termination layer is determined based on the polarization directions of BFO and PTO as well as the polarization catastrophe model. Actually, another polarization configuration (head-to-tail, P_s of PTO point toward BFO, while that of BFO point toward SRO buffer layer, which is not shown here) is identified in the same sample (PTO/BFO/SRO film on the STO substrate).[34] Considering a combination of these two configurations, tail-to-tail polarization is supposed with the $(BiO)^+/(TiO_2)^0$ interface. Since in both the BFO and PTO layers, the polarization directions keep far away from the interface, negative bound charges will accumulate at the interface. If it is a $(FeO_2)^-/(PbO)^0$ interface, the $(FeO_2)^-$ layer, which is also negatively charged, will further aggravate this negative charge accumulation and accelerate a polarization catastrophe, which is energetically unfavorable.

The charge state such as chemical valence, ferroelectric polarization, and charged carriers at oxide interfaces plays a crucial role in determining their physical behaviors,[1,8,13] and therefore, we further analyze the interfacial structure from the perspective of charge distribution. For the head-to-head polarization configuration, a schematic showing interfacial charge characteristic is shown in Figure 5a. First, the chemical valence difference between BFO ($(FeO_2)^-$, $(BiO)^+$) and PTO ($(TiO_2)^0$, $(PbO)^0$) will facilitate interfacial charge reconstruction to avoid polarization catastrophe. According to half electron transfer theory,[50] if 0.5|e|/u.c. exists at the interface, electric potential diverging could be avoided effectively. Here, P_s values in PTO and BFO (along the out-of-plane direction) are calculated to be 83 and 62 $\mu C/cm^2$, respectively,[22,34,51] which equal to 0.83|e| and 0.62|e| per perovskite unit ($1\ \mu C/cm^2 = 1 \times 10^{-22}$ C/A^2 $= 1 \times 10^{-22} \times 3.9^2$ C/u.c. $= 1.6 \times 10^{-21}$ C/u.c. = 0.01|e|/u.c., where, $e = -1.6 \times 10^{-19}$ C, means electron charge; u.c., unit cell). This ferroelectric polarization scenery imposes a polarization bound charge of 0.83|e|/u.c. + 0.62|e|/u.c. = 1.45|e|/u.c. at the interface. In order to compensate for this positive polarization bound charge, and thus avoid polarization catastrophe, the negative charge of 0.95e/u.c. (0.5|e|/u.c. − 1.45|e|/u.c. = 0.95e/u.c.) is needed. Then, the charge configuration at the exact interface is estimated according to the atomic model in Figure 4a: there are 2 Pb^{2+}, 2 Ti^{4+}, 2 Bi^{3+}, 2 Fe^{3+}, and 14 O^{2-} ions in each structural unit, which corresponds to 4e net charge, and equals to 4e/3 in each perovskite unit cell (1.33e/u.c.). A little difference is revealed between the charge value (1.33e/u.c.) calculated based on the atomic model and that calculated based on polar catastrophe (0.95e/u.c.). This may because both models are constructed based on an ideal condition, while a real one may unavoidably have element intermixing, chemical valence (such as Fe and Ti), or ferroelectric polarization variations near the interface.

The charge configuration of the tail-to-tail interfacial domain wall is schematically shown in Figure 5b. This interface exhibits a $(BiO)^+/(TiO_2)^0$ atomic layer arrangement, and we define the $(BiO)^+$ layer as the exact interface here. From the perspective of charge, if the total charge of 0.5|e|/u.c. exists at this valence discontinuous interface, the polar catastrophe could be avoided. Because of the P_s directions in both BFO and PTO pointing away from the interface, it leads to a negative bound charge of

DOI: 10.1021/acsami.7b04681
ACS Appl. Mater. Interfaces 2017, 9, 25578−25586

1.45e/u.c. (0.83e/u.c. + 0.62e/u.c. = 1.45e/u.c.) accumulated at the interface, so there shall be extra 0.5|e|/u.c. − 1.45e/u.c. = 1.95|e|/u.c. to avoid potential diverging. These charges are partly compensated by the $(BiO)^+$ layer (equals to |e|/u.c.). Besides the $(BiO)^+$ layer, some other positive charges are supposed to exist. At the tail-to-tail charged domain wall, oxygen vacancy that is positive charged was suggested to compensate negative polarization bound charge in previous studies.[23] Here, we suppose that it is oxygen vacancy that provides 0.95|e| (1.95|e|/u.c. − 0.95|e|/u.c. = 1|e|/u.c.) in compensating the interfacial negative charge. This is consistent with the lattice elongation in the PTO layer near the BFO/PTO interface that reaches a value of 4.24 Å as shown in Figure 3, since oxygen vacancy inducing lattice expansion in perovskite oxides were experimentally proved by previous work.[34,52]

3.4. Discussion about the Width of the Charged BFO/PTO Interfaces and the Charge Compensation Mechanisms. According to the results and analyses shown above, a reconstructed interfacial structure that is rich in O^{2-} and exhibits a head-to-head polarization configuration is revealed, and its width is estimated to be about 5−6 unit cells. This width value is remarkably smaller than those observed at the head-to-head polarized 180° domain wall in $PbZr_{0.2}Ti_{0.8}O_3$ (∼10 unit cells) and the 90° domain wall in PTO (>10 unit cells).[22,23] This may be a result of a difference in the screening mechanism. The head-to-head 180° domain wall in $PbZr_{0.2}Ti_{0.8}O_3$ has a width of about 10 unit cells. It is proposed that the valence decrease from Ti^{4+} to Ti^{3+} contributes to the charge compensation at this kind of domain wall, and polarization charges distributing over a wide thickness could reduce the system energy.[22] For the positively charged 90° domain wall in PTO, Tang et al. suggested that an oxygen vacancy depletion layer should compensate for the polarization bound charges, and results in a wide domain wall of over 10 unit cells.[23] In the present study, the polarization charge is supposed to be compensated by the extra O^{2-} that is located at the exact reconstructed interface. The O^{2-} is confined at the BFO/PTO interface. As a result, a head-to-head BFO/PTO interface is formed with the width of 5−6 unit cells, narrower than those of the 90° and 180° domain walls in PTO and PZT. Compared to the head-to-head BFO/PTO interface, the tail-to-tail polarized interface identified here is proved narrower (about 3−4 unit cells), and this result is consistent with that of the tail-to-tail polarized 90° domain wall reported in PTO (about 5 unit cells), which is much narrower than the head-to-head one. At this negatively charged 90° domain wall, the positively charged oxygen vacancy is suggested to screen polarization bound charges.[23] Here in our work, we also propose that it is oxygen vacancy that accumulates at the BFO/PTO interface and compensates for the negative polarization charge, which can be proved by the slight expansion of out-of-plane lattice parameters near the BFO/PTO interface, as shown in Figure 3. Furthermore, these accumulated oxygen vacancies, providing n-type carriers ($O_o \rightleftharpoons {}^1/_2O_2+V_o^{\cdot\cdot}+2e'$, where, O_o indicates an oxygen ion on oxygen site, $V_o^{\cdot\cdot}$ denotes a vacant oxygen site, and e' is an electron), may significantly improve the conduction, at the ferroelectric domain walls[14,53,54] and facilitate the formation of 2D electron gas at the valence discontinuous $LaAlO_3/SrTiO_3$ heterointerface.[1]

From the analyses above, it can be revealed that the width of the head-to-head BFO/PTO interface is slightly larger than that of the tail-to-tail one. Besides the difference in interfacial screening mechanisms, two other factors are supposed to affect this width difference as well: one is the head-to-head BFO/PTO interface itself; it deviates from the perovskite structure and has a width of about 1 unit cell; the other, is the particular charge state at the head-to-head BFO/PTO interface. According to the calculations shown above, the charge value (1.33e/u.c.) based on the atomic model is larger than that needed to avoid polar catastrophe (0.95e/u.c.). This charge difference may be compensated by some interfacial intermixing around the BFO/PTO interface, causing the broadening of this charged interface.

3.5. Formation of the Distinct Interfacial Configurations. Here, we consider that the ferroelectric polarization direction of BFO plays significant roles in determining the interfacial structure. When ultrathin BFO (∼10 u.c.) films grow directly on STO substrates, an upward polarization is adopted, which will introduce positive charge accumulation at the BFO/PTO interface and facilitate the reconstructed and O^{2-} rich interface, as shown in Figures 1 and 2. However, when a SRO buffer layer is added, the work function difference between SRO and BFO (SRO ∼ 4.9 eV, BFO ∼ 3.3 eV)[55,56] results in a built-in electric field pointing toward SRO at the BFO/SRO interface, thus giving rise to a ferroelectric polarization of BFO pointing toward SRO, which is in agreement with the previous report in BFO film grown epitaxially on a SRO buffered STO substrate.[46] Then, negative charge will accumulate at the BFO/PTO interface and may facilitate the formation of a positively charged oxygen vacancy and lead to a coherence interface as shown in Figure 3.

4. CONCLUSIONS

In summary, by properly engineering the film system, head-to-head positively charged and tail-to-tail negatively charged BFO/PTO interfaces are successfully obtained. Aberration-corrected STEM investigation reveals that, when BFO/PTO is deposited directly on a STO (001) substrate, a head-to-head polarization configuration is adopted around this heterointerface, showing a reconstructed interfacial structure deviating largely from the perovskite which is rich in O^{2-}. The negatively charged O^{2-} is supposed to compensate for the positive polarization bound charges induced by the head-to-head polarization. The width of this interface is estimated to be about 5−6 unit cells as a result of interfacial structural and charge reconstruction. In parallel, a tail-to-tail BFO/PTO interface is obtained by depositing BFO/PTO film on a SRO buffered STO (001) substrate. In contrast to the reconstructed interface for a head-to-head polarization configuration, this interface is coherent, and its width is estimated to be 3−4 unit cells. At this interface, an oxygen vacancy is suggested to screen negative bound charges induced by the tail-to-tail polarization. The controlled growth and the atomic-scale investigation of these heterointerfaces may facilitate the further exploration of their properties and applications in an electronic device.

AUTHOR INFORMATION

Corresponding Author

*E-mail: ylzhu@imr.ac.cn.

ORCID

Yin-Lian Zhu: 0000-0002-0356-3306

Jagadeesh Suriyaprakash: 0000-0001-7269-2841

Notes

The authors declare no competing financial interest.

DOI: 10.1021/acsami.7b04681
ACS Appl. Mater. Interfaces 2017, 9, 25578−25586

■ ACKNOWLEDGMENTS

This work is supported by the National Natural Science Foundation of China (nos. 51231007, 51571197, 51501194, 51671194, and 51521091), National Basic Research Program of China (2014CB921002), and the Key Research Program of Frontier Sciences CAS (QYZDJ-SSW-JSC010). Y. L. Tang acknowledges the IMR SYNL-T.S. Kê Research Fellowship and the Youth Innovation Promotion Association CAS (no. 2016177). The authors are grateful to B. Wu and L.X. Yang of this laboratory for their technical supports on the Titan platform of the G2 60-300 kV aberration-corrected scanning transmission electron microscope.

■ REFERENCES

(1) Ohtomo, A.; Hwang, H. Y. A high-Mobility Electron Gas at the $LaAlO_3/SrTiO_3$ Heterointerface. *Nature* **2004**, *427*, 423−426.
(2) Reyren, N.; Thiel, S.; Caviglia, A. D.; Kourkoutis, L. F.; Hammerl, G.; Richter, C.; Schneider, C. W.; Kopp, T.; Ruetschi, A. S.; Jaccard, D.; Gabay, M.; Muller, D. A.; Triscone, J. M.; Mannhart, J. Superconducting Interfaces Between Insulating Oxides. *Science* **2007**, *317*, 1196−1199.
(3) Zheng, H.; Wang, J.; Lofland, S. E.; Ma, Z.; Mohaddes-Ardabili, L.; Zhao, T.; Salamanca-Riba, L.; Shinde, S. R.; Ogale, S. B.; Bai, F.; Viehland, D.; Jia, Y.; Schlom, D. G.; Wuttig, M.; Roytburd, A.; Ramesh, R. Multiferroic $BaTiO_3$-$CoFe_2O_4$ Nanostructures. *Science* **2004**, *303*, 661−663.
(4) Garcia, V.; Bibes, M.; Bocher, L.; Valencia, S.; Kronast, F.; Crassous, A.; Moya, X.; Enouz-Vedrenne, S.; Gloter, A.; Imhoff, D.; Deranlot, C.; Mathur, N. D.; Fusil, S.; Bouzehouane, K.; Barthelemy, A. Ferroelectric Control of Spin Polarization. *Science* **2010**, *327*, 1106−1110.
(5) Duan, C. G.; Jaswal, S. S.; Tsymbal, E. Y. Predicted Magnetoelectric Effect in $Fe/BaTiO_3$ Multilayers: Ferroelectric Control of Magnetism. *Phys. Rev. Lett.* **2006**, *97*, 047201.
(6) Liu, X.; Wang, Y.; Burton, J. D.; Tsymbal, E. Y. Polarization-Controlled Ohmic to Schottky Transition at a Metal/Ferroelectric Interface. *Phys. Rev. B: Condens. Matter Mater. Phys.* **2013**, *88*, 165139.
(7) Yin, Y. W.; Burton, J. D.; Kim, Y. M.; Borisevich, A. Y.; Pennycook, S. J.; Yang, S. M.; Noh, T. W.; Gruverman, A.; Li, X. G.; Tsymbal, E. Y.; Li, Q. Enhanced Tunnelling Electroresistance Effect Due to a Ferroelectrically Induced Phase Transition at a Magnetic Complex Oxide Interface. *Nat. Mater.* **2013**, *12*, 397−402.
(8) Maksymovych, P.; Jesse, S.; Yu, P.; Ramesh, R.; Baddorf, A. P.; Kalinin, S. V. Polarization Control of Electron Tunneling into Ferroelectric Surfaces. *Science* **2009**, *324*, 1421−1425.
(9) Pantel, D.; Goetze, S.; Hesse, D.; Alexe, M. Reversible Electrical Switching of Spin Polarization in Multiferroic Tunnel Junctions. *Nat. Mater.* **2012**, *11*, 289−293.
(10) Martin, L. W.; Chu, Y. H.; Holcomb, M. B.; Huijben, M.; Yu, P.; Han, S. J.; Lee, D.; Wang, S. X.; Ramesh, R. Nanoscale Control of Exchange Bias with $BiFeO_3$ Thin Films. *Nano Lett.* **2008**, *8*, 2050−2055.
(11) Daraktchiev, M.; Catalan, G.; Scott, J. F. Landau Theory of Domain Wall Magnetoelectricity. *Phys. Rev. B: Condens. Matter Mater. Phys.* **2010**, *81*, 224118.
(12) Seidel, J.; Martin, L. W.; He, Q.; Zhan, Q.; Chu, Y. H.; Rother, A.; Hawkridge, M. E.; Maksymovych, P.; Yu, P.; Gajek, M.; Balke, N.; Kalinin, S. V.; Gemming, S.; Wang, F.; Catalan, G.; Scott, J. F.; Spaldin, N. A.; Orenstein, J.; Ramesh, R. Conduction at Domain Walls in Oxide Multiferroics. *Nat. Mater.* **2009**, *8*, 229−234.
(13) Meier, D.; Seidel, J.; Cano, A.; Delaney, K.; Kumagai, Y.; Mostovoy, M.; Spaldin, N. A.; Ramesh, R.; Fiebig, M. Anisotropic Conductance at Improper Ferroelectric Domain Walls. *Nat. Mater.* **2012**, *11*, 284−288.
(14) Guyonnet, J.; Gaponenko, I.; Gariglio, S.; Paruch, P. Conduction at Domain Walls in Insulating $Pb(Zr_{0.2}Ti_{0.8})O_3$ Thin Films. *Adv. Mater.* **2011**, *23*, 5377−5382.
(15) Xu, T.; Shimada, T.; Araki, Y.; Wang, J.; Kitamura, T. Multiferroic Domain Walls in Ferroelectric $PbTiO_3$ with Oxygen Deficiency. *Nano Lett.* **2016**, *16*, 454−458.
(16) Catalan, G.; Seidel, J.; Ramesh, R.; Scott, J. F. Domain Wall Nanoelectronics. *Rev. Mod. Phys.* **2012**, *84*, 119−156.
(17) He, Q.; Yeh, C. H.; Yang, J. C.; Singh-Bhalla, G.; Liang, C. W.; Chiu, P. W.; Catalan, G.; Martin, L. W.; Chu, Y. H.; Scott, J. F.; Ramesh, R. Magnetotransport at Domain Walls in $BiFeO_3$. *Phys. Rev. Lett.* **2012**, *108*, 067203.
(18) Vul, B. M.; Guro, G. M.; Ivanchik, I. I. Encountering Domains in Ferroelectrics. *Ferroelectrics* **1973**, *6*, 29−31.
(19) Bednyakov, P.; Sluka, T.; Tagantsev, A.; Damjanovic, D.; Setter, N. Free-Carrier-Compensated Charged Domain Walls Produced with Super-Bandgap Illumination in Insulating Ferroelectrics. *Adv. Mater.* **2016**, *28*, 9498−9503.
(20) Eliseev, E. A.; Morozovska, A. N.; Svechnikov, G. S.; Gopalan, V.; Shur, V. Y. Static Conductivity of Charged Domain Walls in Uniaxial Ferroelectric Semiconductors. *Phys. Rev. B: Condens. Matter Mater. Phys.* **2011**, *83*, 235313.
(21) Sluka, T.; Tagantsev, A. K.; Damjanovic, D.; Gureev, M.; Setter, N. Enhanced Electromechanical Response of Ferroelectrics Due to Charged Domain Dalls. *Nat. Commun.* **2012**, *3*, 748.
(22) Jia, C. L.; Mi, S. B.; Urban, K.; Vrejoiu, I.; Alexe, M.; Hesse, D. Atomic-Scale Study of Electric Dipoles near Charged and Uncharged Domain Walls in Ferroelectric Films. *Nat. Mater.* **2008**, *7*, 57−61.
(23) Tang, Y. L.; Zhu, Y. L.; Wang, Y. J.; Wang, W. Y.; Xu, Y. B.; Ren, W. J.; Zhang, Z. D.; Ma, X. L. Atomic-Scale Mapping of Dipole Frustration at 90 Degrees Charged Domain Walls in Ferroelectric $PbTiO_3$ Films. *Sci. Rep.* **2014**, *4*, 4115.
(24) Wang, W. Y.; Tang, Y. L.; Zhu, Y. L.; Xu, Y. B.; Liu, Y.; Wang, Y.-J.; Jagadeesh, S.; Ma, X.-L. Atomic Level 1D Structural Modulations at the Negatively Charged Domain Walls in $BiFeO_3$ Films. *Adv. Mater. Interfaces* **2015**, *2*, 1500024.
(25) Li, L.; Gao, P.; Nelson, C. T.; Jokisaari, J. R.; Zhang, Y.; Kim, S.-J.; Melville, A.; Adamo, C.; Schlom, D. G.; Pan, X. Atomic Scale Structure Changes Induced by Charged Domain Walls in Ferroelectric Materials. *Nano Lett.* **2013**, *13*, 5218−5223.
(26) Anbusathaiah, V.; Kan, D.; Kartawidjaja, F. C.; Mahjoub, R.; Arredondo, M. A.; Wicks, S.; Takeuchi, I.; Wang, J.; Nagarajan, V. Labile Ferroelastic Nanodomains in Bilayered Ferroelectric Thin Films. *Adv. Mater.* **2009**, *21*, 3497−3502.
(27) Huang, H. H.; Hong, Z. J.; Xin, H. L. L.; Su, D.; Chen, L. Q.; Huang, G. Z.; Munroe, P. R.; Valanoor, N. Nanoscale Origins of Ferroelastic Domain Wall Mobility in Ferroelectric Multilayers. *ACS Nano* **2016**, *10*, 10126−10134.
(28) Sharma, S.; Tomar, M.; Kumar, A.; Puri, N. K.; Gupta, V. Multiferroic Properties of $BiFeO_3/BaTiO_3$ Multilayered Thin Films. *Phys. B* **2014**, *448*, 125−127.
(29) Gupta, R.; Chaudhary, S.; Kotnala, R. K. Interfacial Charge Induced Magnetoelectric Coupling at $BiFeO_3/BaTiO_3$ Bilayer Interface. *ACS Appl. Mater. Interfaces* **2015**, *7*, 8472−8479.
(30) Kotnala, R. K.; Gupta, R.; Chaudhary, S. Giant Magnetoelectric Coupling Interaction in $BaTiO_3/BiFeO_3/BaTiO_3$ Trilayer Multiferroic Heterostructures. *Appl. Phys. Lett.* **2015**, *107*, 082908.
(31) Ramesh, R.; Zavaliche, F.; Chu, Y. H.; Martin, L. W.; Yang, S. Y.; Cruz, M. P.; Barry, M.; Lee, K.; Yang, P.; Zhan, Q. Magnetoelectric Complex-Oxide Heterostructures. *Philos. Mag. Lett.* **2007**, *87*, 155−164.
(32) Sinsheimer, J.; Callori, S. J.; Bein, B.; Benkara, Y.; Daley, J.; Coraor, J.; Su, D.; Stephens, P. W.; Dawber, M. Engineering Polarization Rotation in a Ferroelectric Superlattice. *Phys. Rev. Lett.* **2012**, *109*, 167601.
(33) Hong, L.; Wu, P.; Li, Y.; Gopalan, V.; Eom, C.-B.; Schlom, D. G.; Chen, L.-Q. Piezoelectric Enhancement of $(PbTiO_3)_{(m)}/(BaTiO_3)_{(n)}$ Ferroelectric Superlattices Through Domain Engineering. *Phys. Rev. B: Condens. Matter Mater. Phys.* **2014**, *90*, 174111.
(34) Liu, Y.; Zhu, Y. L.; Tang, Y. L.; Wang, Y. J.; Jiang, Y. X.; Xu, Y. B.; Zhang, B.; Ma, X. L. Local Enhancement of Polarization at

DOI: 10.1021/acsami.7b04681
ACS Appl. Mater. Interfaces 2017, 9, 25578−25586

$PbTiO_3/BiFeO_3$ Interfaces Mediated by Charge Transfer. *Nano Lett.* **2017**, *17*, 3619.
(35) Kim, Y. M.; Morozovska, A.; Eliseev, E.; Oxley, M. P.; Mishra, R.; Selbach, S. M.; Grande, T.; Pantelides, S. T.; Kalinin, S. V.; Borisevich, A. Y. Direct Observation of Ferroelectric Field Effect and Vacancy-Controlled Screening at the $BiFeO_3/La_xSr_{1-x}MnO_3$ Interface. *Nat. Mater.* **2014**, *13*, 1019−1025.
(36) Lee, P. W.; Singh, V. N.; Guo, G. Y.; Liu, H. J.; Lin, J. C.; Chu, Y. H.; Chen, C. H.; Chu, M. W. Hidden Lattice Instabilities as Origin of the Conductive Interface Between Insulating $LaAlO_3$ and $SrTiO_3$. *Nat. Commun.* **2016**, *7*, 12773.
(37) Tang, Y. L.; Zhu, Y. L.; Ma, X. L.; Borisevich, A. Y.; Morozovska, A. N.; Eliseev, E. A.; Wang, W. Y.; Wang, Y. J.; Xu, Y. B.; Zhang, Z. D.; Pennycook, S. J. Observation of a Periodic Array of Flux-Closure Quadrants in Strained Ferroelectric $PbTiO_3$ Films. *Science* **2015**, *348*, 547−551.
(38) Yadav, A. K.; Nelson, C. T.; Hsu, S. L.; Hong, Z.; Clarkson, J. D.; Schlepütz, C. M.; Damodaran, A. R.; Shafer, P.; Arenholz, E.; Dedon, L. R.; Chen, D.; Vishwanath, A.; Minor, A. M.; Chen, L. Q.; Scott, J. F.; Martin, L. W.; Ramesh, R. Observation of Polar Vortices in Oxide Superlattices. *Nature* **2016**, *530*, 198−201.
(39) Anthony, S. M.; Granick, S. Image Analysis with Rapid and Accurate Two-Dimensional Gaussian Fitting. *Langmuir* **2009**, *25*, 8152−8160.
(40) Glazer, A. M.; Mabud, S. A. Powder Profile Refinement of Lead Zirconate Titanate at Several Temperatures. 2. Pure $PbTiO_3$. *Acta Crystallogr., Sect. B: Struct. Crystallogr. Cryst. Chem.* **1978**, *34*, 1065−1070.
(41) Kubel, F.; Schmid, H. Structure of a Ferroelectric and Ferroelastic Monodomain Crystal of the Perovskite $BiFeO_3$. *Acta Crystallogr., Sect. B: Struct. Sci.* **1990**, *46*, 698−702.
(42) Michel, C.; Moreau, J.-M.; Achenbach, G. D.; Gerson, R.; James, W. J. Atomic Structure of $BiFeO_3$. *Solid State Commun.* **1969**, *7*, 701−704.
(43) Nelson, C. T.; Winchester, B.; Zhang, Y.; Kim, S. J.; Melville, A.; Adamo, C.; Folkman, C. M.; Baek, S. H.; Eom, C. B.; Schlom, D. G.; Chen, L. Q.; Pan, X. Q. Spontaneous Vortex Nanodomain Arrays at Ferroelectric Heterointerfaces. *Nano Lett.* **2011**, *11*, 828−834.
(44) Wang, W. Y.; Zhu, Y. L.; Tang, Y. L.; Xu, Y. B.; Liu, Y.; Li, S.; Zhang, S. R.; Wang, Y. J.; Ma, X. L. Large Scale Arrays of Four-State Vortex Domains in $BiFeO_3$ Thin Film. *Appl. Phys. Lett.* **2016**, *109*, 202904.
(45) Wang, W. Y.; Tang, Y. L.; Zhu, Y. L.; Xu, Y. B.; Liu, Y.; Wang, Y. J.; Jagadeesh, S.; Ma, X. L. Atomic Level 1D Structural Modulations at the Negatively Charged Domain Walls in $BiFeO_3$ Films. *Adv. Mater. Interfaces* **2015**, *2*, 1500024.
(46) Liu, Y.; Zhu, Y. L.; Tang, Y. L.; Ma, X. L. An Effect of Crystal Tilt on the Determination of Ions Displacements in Peroveskite Oxides under HAADF/BF-STEM Imaging Mode. *J. Mater. Res.* **2017**, *32*, 947−956.
(47) Jia, C. L.; Urban, K. W.; Alexe, M.; Hesse, D.; Vrejoiu, I. Direct Observation of Continuous Electric Dipole Rotation in Flux-Closure Domains in Ferroelectric $Pb(Zr,Ti)O_3$. *Science* **2011**, *331*, 1420−1423.
(48) MacLaren, I.; Wang, L. Q.; Morris, O.; Craven, A. J.; Stamps, R. L.; Schaffer, B.; Ramasse, Q. M.; Miao, S.; Kalantari, K.; Sterianou, I.; Reaney, I. M. Local Stabilisation of Polar Order at Charged Antiphase Boundaries in Antiferroelectric $(Bi_{0.85}Nd_{0.15})(Ti_{0.1}Fe_{0.9})O_3$. *APL Mater.* **2013**, *1*, 021102.
(49) Farokhipoor, S.; Noheda, B. Conduction Through 71 Degrees Domainwalls in $BiFeO_3$ Thin Films. *Phys. Rev. Lett.* **2011**, *107*, 127601.
(50) Nakagawa, N.; Hwang, H. Y.; Muller, D. A. Why Some Interfaces Cannot be Sharp. *Nat. Mater.* **2006**, *5*, 204−209.
(51) Zhong, W.; Kingsmith, R. D.; Vanderbilt, D. Giant LO-TO Splittings in Perovskite Ferroelectrics. *Phys. Rev. Lett.* **1994**, *72*, 3618−3621.
(52) Kim, Y. M.; He, J.; Biegalski, M. D.; Ambaye, H.; Lauter, V.; Christen, H. M.; Pantelides, S. T.; Pennycook, S. J.; Kalinin, S. V.; Borisevich, A. Y. Probing Oxygen Vacancy Concentration and Homogeneity in Solid-Oxide Fuel-Cell Cathode Materials on the Subunit-cell Level. *Nat. Mater.* **2012**, *11*, 888−894.
(53) Wu, W. D.; Horibe, Y.; Lee, N.; Cheong, S. W.; Guest, J. R. Conduction of Topologically Protected Charged Ferroelectric Domain Walls. *Phys. Rev. Lett.* **2012**, *108*, 077203.
(54) Seidel, J.; Maksymovych, P.; Batra, Y.; Katan, A.; Yang, S.-Y.; He, Q.; Baddorf, A. P.; Kalinin, S. V.; Yang, C.-H.; Yang, J.-C.; Chu, Y.-H.; Salje, E. K. H.; Wormeester, H.; Salmeron, M.; Ramesh, R. Domain Wall Conductivity in La-Doped $BiFeO_3$. *Phys. Rev. Lett.* **2010**, *105*, 197603.
(55) Gao, P.; Nelson, C. T.; Jokisaari, J. R.; Zhang, Y.; Baek, S. H.; Bark, C. W.; Wang, E.; Liu, Y. M.; Li, J. Y.; Eom, C. B.; Pan, X. Q. Direct Observations of Retention Failure in Ferroelectric Memories. *Adv. Mater.* **2012**, *24*, 1106−1110.
(56) Moubah, R.; Rousseau, O.; Colson, D.; Artemenko, A.; Maglione, M.; Viret, M. Photoelectric Effects in Single Domain $BiFeO_3$ Crystals. *Adv. Funct. Mater.* **2012**, *22*, 4814−4818.

DOI: 10.1021/acsami.7b04681
ACS Appl. Mater. Interfaces 2017, 9, 25578−25586